



Chinese Pharmaceutical Association  
Institute of Materia Medica, Chinese Academy of Medical Sciences

Acta Pharmaceutica Sinica B

[www.elsevier.com/locate/apsb](http://www.elsevier.com/locate/apsb)  
[www.sciencedirect.com](http://www.sciencedirect.com)



ORIGINAL ARTICLE

# Computer-aided molecular design and optimization of potent inhibitors disrupting APC–Asef interaction



Xuefei Wang<sup>a,b,†</sup>, Zeqian Du<sup>c,†</sup>, Yuegui Guo<sup>d,†</sup>, Jie Zhong<sup>a,†</sup>,  
Kun Song<sup>a</sup>, Junyuan Wang<sup>b</sup>, Jianqiang Yu<sup>b</sup>, Xiuyan Yang<sup>a,e,\*</sup>,  
Chen-Ying Liu<sup>d,\*</sup>, Ting Shi<sup>c,\*</sup>, Jian Zhang<sup>a,b,f,g,\*</sup>

<sup>a</sup>Department of Pathophysiology, Key Laboratory of Cell Differentiation and Apoptosis of Chinese Ministry of Education, Shanghai Jiao Tong University, School of Medicine, Shanghai 200025, China

<sup>b</sup>Key Laboratory of Protection, Development and Utilization of Medicinal Resources in Liupanshan Area, Ministry of Education, Peptide & Protein Drug Research Center, School of Pharmacy, Ningxia Medical University, Yinchuan 750004, China

<sup>c</sup>State Key Laboratory of Microbial Metabolism, Joint International Research Laboratory of Metabolic and Developmental Sciences, School of Life Sciences and Biotechnology, Shanghai Jiao Tong University, Shanghai 200240, China

<sup>d</sup>Department of Colorectal and Anal Surgery, Xinhua Hospital, Shanghai Jiao Tong University School of Medicine, Shanghai 200025, China

<sup>e</sup>Basic Science Research Center Base (Pharmaceutical Science), Yantai University, Yantai 264005, China

<sup>f</sup>Medicinal Chemistry and Bioinformatics Center, Shanghai Jiao Tong University, School of Medicine, Shanghai 200025, China

<sup>g</sup>State Key Laboratory of Pharmaceutical Biotechnology, Nanjing University, Nanjing 210023, China

Received 16 October 2023; received in revised form 4 March 2024; accepted 14 March 2024

## KEY WORDS

APC–Asef;  
Peptidomimetic;  
Computer-aided molecular  
design;

**Abstract** Colorectal cancer (CRC) is the second leading cause of cancer mortality worldwide. At initial diagnosis, approximately 20% of patients are diagnosed with metastatic CRC (mCRC). Although the APC–Asef interaction is a well-established target for mCRC therapy, the discovery and development of effective and safe drugs for mCRC patients remains an urgent and challenging endeavor. In this study, we identified a novel structural scaffold based on MAI inhibitors, the first-in-class APC–Asef inhibitors

\*Corresponding authors.

E-mail addresses: [shanshiyan@126.com](mailto:shanshiyan@126.com) (Xiuyan Yang), [liuchenying@xinhumed.com.cn](mailto:liuchenying@xinhumed.com.cn) (Chen-Ying Liu), [tshi@sjtu.edu.cn](mailto:tshi@sjtu.edu.cn) (Ting Shi), [jian.zhang@sjtu.edu.cn](mailto:jian.zhang@sjtu.edu.cn) (Jian Zhang).

<sup>†</sup>These authors made equal contributions to this work.

Peer review under the responsibility of Chinese Pharmaceutical Association and Institute of Materia Medica, Chinese Academy of Medical Sciences.

<https://doi.org/10.1016/j.apsb.2024.03.020>

2211-3835 © 2024 The Authors. Published by Elsevier B.V. on behalf of Chinese Pharmaceutical Association and Institute of Materia Medica, Chinese Academy of Medical Sciences. This is an open access article under the CC BY-NC-ND license (<http://creativecommons.org/licenses/by-nc-nd/4.0/>).

ONIOM model;  
 $\pi$ - $\pi$  stacking;  
 Metastatic colorectal  
 cancer

we reported previously. ONIOM model-driven optimizations of the N-terminal cap and experimental evaluations of inhibitory activity were performed, and 24-fold greater potency was obtained with the best inhibitor compared to the parental compound. In addition, the cocrystal structure validated that the two-layer  $\pi$ - $\pi$  stacking interactions were essential for inhibitor stabilization in the bound state. Furthermore, *in vitro* and *in vivo* studies have demonstrated that novel inhibitors suppressed lung metastasis in CRC by disrupting the APC-Asef interaction. These results provide an intrinsic structural basis to further explore drug-like molecules for APC-Asef-mediated CRC therapy.

© 2024 The Authors. Published by Elsevier B.V. on behalf of Chinese Pharmaceutical Association and Institute of Materia Medica, Chinese Academy of Medical Sciences. This is an open access article under the CC BY-NC-ND license (<http://creativecommons.org/licenses/by-nc-nd/4.0/>).

## 1. Introduction

Colorectal cancer (CRC) is the third most common cancer and the second leading cause of cancer mortality worldwide, with an estimated 1.9 million cases and almost 0.9 million deaths in 2020<sup>1</sup>. Metastasis is the major cause of death in most patients with CRC and occurs in approximately 20% of patients at initial diagnosis and 50% of patients with localized disease<sup>2</sup>. The prognosis of metastatic CRC (mCRC) remains poor, with an overall 5-year survival rate of less than 20%<sup>3</sup>. Although major efforts have been dedicated to the molecular characterization of mCRC and some druggable targets for personalized treatments have been identified, relatively few novel drugs have been introduced into mCRC therapy<sup>4-7</sup>.

The standard first-line treatment for patients with mCRC is fluoropyrimidine-based (FOLFOX/CAPOX or FOLFIRI/CAPIRI) chemotherapy<sup>8,9</sup>. Hence, the development of effective and safe drugs for mCRC therapy is crucial. CRC typically originates from polyps in the colon or rectum. Mutations in adenomatous polyposis coli (APC) are the initial events in mCRC development<sup>10</sup>. Under normal physiologic conditions, APC functions as a tumor suppressor and is responsible for proteasomal degradation of  $\beta$ -catenin in the canonical Wnt pathway<sup>11</sup>. APC is involved in various cellular processes related to cell adhesion, migration, proliferation, and differentiation<sup>12</sup>. Most mutations in APC produce truncated proteins in CRC tumorigenesis. Truncated APC retains an oligomerization domain named an armadillo repeat-domain (ARM), which is the most conserved domain in the APC protein<sup>13</sup>. ARM provides a specific binding site for Rho guanine nucleotide exchange factor 4 (Asef). The interaction between truncated APC and Asef relieves the negative intramolecular regulation of Asef, resulting in an overactivated state of the downstream cell division cycle 42 (CDC42) with subsequent signaling cascades; these events promote aberrant migration and invasion of CRC cells<sup>14-16</sup>. Moreover, knockdown of APC or Asef significantly reduced migration in several CRC cell lines with truncated APC<sup>17</sup>. Therefore, the APC-Asef interaction provides a promising therapeutic target for mCRC treatment.

In previous studies, we developed the first class of inhibitors targeting the APC-Asef interaction<sup>18</sup>. In the discovery and characterization of linear peptide inhibitors, the sequence containing seven hotspot residues from Asef was first identified as the starting template for structural modifications. After several rounds of optimizations for side-chain substitutions, a first-in-class inhibitor MAI-203 (<sup>181</sup>AGEA(CP)YE<sup>187</sup>) was produced. Moreover, the introduction of intramolecular hydrogen bonds into the peptide

backbone resulted in MAI-400 (<sup>181</sup>AGESLYE<sup>187</sup>) with higher binding affinity<sup>19</sup>. In an effort to further improve activity, we subsequently optimized the tracers in FP assays for APC-Asef inhibitor screening<sup>20</sup>. When sensitivity-enhanced tracer 7 was applied, MAI-400 exhibited an IC<sub>50</sub> of 2.76  $\mu$ mol/L.

Despite this improvement, the druggability and developability of APC-Asef peptide inhibitors remains challenging. The reported peptides typically contain natural amino acids that are easily hydrolyzed by the proteasome, which leads to poor metabolic stability in plasma. Additionally, cell-penetrating peptides (CPPs) are typically needed for the series of MAI inhibitors to enter cells and exert antimigration functions. Unfortunately, most CPPs suffer from a lack of selectivity for target lesions, which may affect the normal intracellular metabolic pathways and induce serious toxicity as well as side effects<sup>21-27</sup>. Therefore, an important direction toward the development of inhibitors for APC-Asef-mediated CRC therapy may be novel backbone inhibitors without CPPs that exhibit higher inhibitory activity and more drug-like properties.

Herein, we selected MAI-400 as the parental compound and employed a rational design strategy to improve the potency of APC-Asef inhibitors. Structure-based terminal capping modification was combined with ONIOM model-driven optimization for  $\pi$ - $\pi$  stacking in a novel structural scaffold derived from truncated MAI-400. As a result, the best inhibitor was obtained with a 24-fold greater potency than that of MAI-400. Moreover, we developed an inhibitor with esterified modification that could inhibit the colon cancer migration mediated by APC-Asef without TAT support *in vivo*. Collectively, our study provides a novel inhibitor that disrupts the APC-Asef interaction and sheds light on the structural basis for further development of drug-like molecules in mCRC treatment.

## 2. Results and discussion

### 2.1. Design of a novel inhibitor scaffold targeting the APC-Asef interaction

In structure-based drug design, the conformational entropy of ligands is crucial for protein binding. Since each rotatable bond contributes approximately 5–6 kJ/mol to the free energy, reducing the number of rotatable bonds can correspondingly enhance the molecular rigidity and binding affinity<sup>28-31</sup>. Therefore, we attempted to simplify the molecular structure by truncating the parental molecule, MAI-400, which contains the most pivotal bioactive sequence as the original backbone.

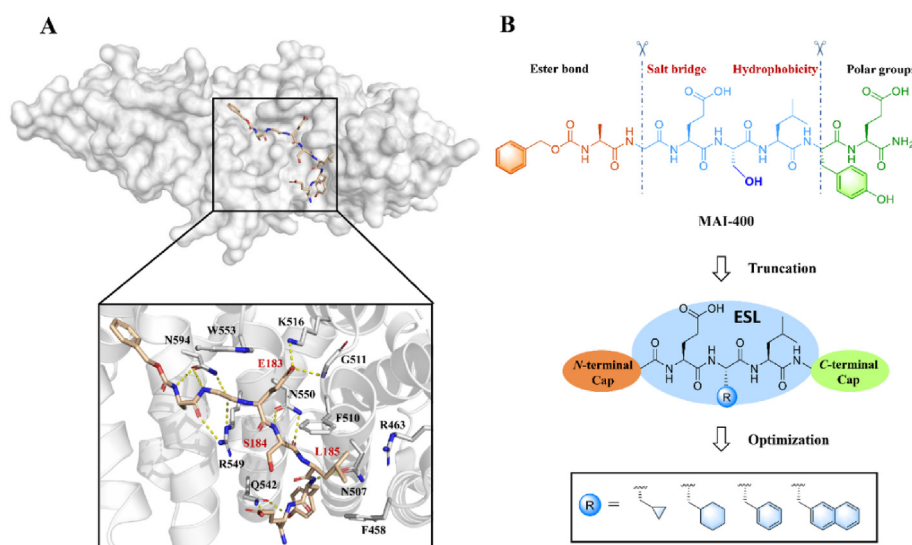
The structural analysis for the binding mode of MAI-400 with APC (Fig. 1A) demonstrated that E183 containing an acidic group acts *via* a salt bridge and hydrogen bond networks with K516 and G511<sup>19</sup>. Hence, E183 was selected as the key residue for retaining inhibitory potency. Additionally, the isobutyl of L185 is another crucial moiety that anchors the APC interface, which inserts into a hydrophobic cavity formed by F510, R463, and F458. Previous SAR studies have shown that this pocket is rigid and difficult to induce<sup>18,19</sup>. Thus, L185 should help retain the high binding affinity. Ser184 participated in the intramolecular hydrogen bond, which was critical for stabilizing the MAI-400-bound conformation. The core sequence for E<sup>183</sup>S<sup>184</sup>L<sup>185</sup> (ESL) was stuck in the cavity of the APC surface as a U-shaped backbone, which was responsible for the complementary shape of the binding protein. The carbamate in the N-terminus is highly specific for carboxylesterase hydrolysis, and elastase easily recognizes and hydrolyzes residues A and G; thus, we decided to remove these segments (Fig. 1B)<sup>32–34</sup>. Considering potential drug-like properties, other residues (Y and E) adjacent to the C-terminus containing some unfavorable polar groups in side chains are eliminated for further molecular modifications. Therefore, the central sequence ESL, namely, AT1, was identified by simplifying the parental MAI-400 that served as the scaffold for subsequent optimization (Table 1).

Chemically modifying the terminal cap of target peptides is a promising strategy to achieve specific peptidomimetic inhibitors. Unprotected peptides with naked N- or C-termini are easily cleaved and degraded by exopeptidases upon their recognition. Studies have shown that introducing capping groups can not only facilitate the metabolic stability of peptide drugs but also enhances their bioactivity<sup>35–38</sup>. Thus, we decided to add terminal capping groups for the first-round optimization of inhibitors. By analyzing the surrounding MAI-400 residues at the bound site, we found that the N-terminus of AT1 was near hydrophobic W553 of the APC pocket. Therefore, we sought to adopt the  $\pi$ - $\pi$  interaction-based design strategy for inhibitor optimization. Reportedly, the presence of the heteroatom may help form a stronger  $\pi$ - $\pi$  interaction compared to that of benzene<sup>39</sup>. Given that the pyrimidine group

serves as a generally used fragment in drug design, we first introduced 4-pyrimidinecarboxylic acid in the inhibitor as an N-terminal cap and synthesized AT2 (Table 1), which showed very weak inhibition. The molecular backbone might not be large enough to anchor the extensive PPI interface, making it difficult to induce a potentially targetable binding pocket. To compensate for the loss of activity by heptapeptide truncation efforts, we focused on modifying the C-terminal cap. The crystal structure revealed that the side chain of Y186 can form hydrophobic interactions with M503. We next synthesized AT3 ( $IC_{50}$  = 323  $\mu$ mol/L) and AT4 (13% inhibition at 400  $\mu$ mol/L) and attempted to extend the benzene moiety by a two-carbon linker to simulate the phenolic conformation of Y186 (Table 1). However, the results suggested that the flexibility of the aliphatic linker resulted in an undesirable binding affinity. Considering that the rigid cyclopropane may restrict the orientation of substituents, we attempted *cis*- and *trans*-phenyl-cyclopropanamine to cap the C-terminus of inhibitors and produced AT5 and AT6. In particular, the *trans*-configuration fragment provides strong binding affinity for the hydrophobic region. Taken together, the results indicate that by simplifying the molecular shape and terminal cap, we produced a promising novel inhibitor AT6 with an  $IC_{50}$  value of 27  $\mu$ mol/L.

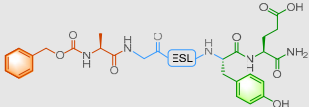

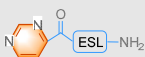
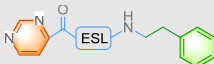
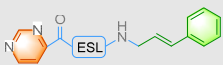

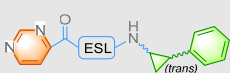
## 2.2. Structure-based modification of hydroxy moiety in inhibitors

To enhance the binding affinity of AT6, we decided to optimize the inhibitor by inserting rigid unnatural moieties into the backbone (Fig. 1B). Structure analysis of MAI-400 in the bound state revealed that the hydroxymethyl of S184 was mainly exposed in the solvent (Fig. 1A). Thus, four new inhibitors (AT7–AT10) with different aliphatic and aromatic substituents on the side chain of S184 (R) were synthesized (Table 2). By adopting larger hydrophobic groups, it was possible to transform the conformation of the binding pocket by an induced fit effect. In addition, steric hindrance was introduced in the cleavage site to delay proteolytic degradation. Notably, the results showed that binding affinity was diminished when R was replaced with cyclopropyl (AT7),



**Figure 1** Identification of the tripeptide template. (A) Selection of tripeptide derived from the central “U” scaffold of MAI-400 (crystal structure of APC in complex with MAI-400, PDB code 5Z8H, resolution 1.79 Å). The MAI-400 backbone is represented by a wheat stick, and the APC protein is represented by a gray surface. (B) Workflow for the optimization of MAI-400.


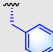

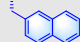
**Table 1** Inhibitory activity of MAI-400 and compounds AT1–6<sup>a</sup> targeting APC–Asef.

Compd.	Structure	Inhibitory activity
MAI-400		97.1 ± 0.5% at 100 μmol/L
AT1		N.A. <sup>b</sup>
AT2		11.2 ± 1.0%
AT3		54.6 ± 2.0%
AT4		13.1 ± 0.7%
AT5		N.A. <sup>b</sup>
AT6		95.1 ± 0.9%

<sup>a</sup>The inhibition rate % at 400 μmol/L of the compounds AT1–6 in the fluorescence-polarization (FP) competition assay were assessed as described in the Experimental Section.

<sup>b</sup>N.A. means not available.

**Table 2** Inhibitory activity of compounds AT7–10 targeting APC–Asef.

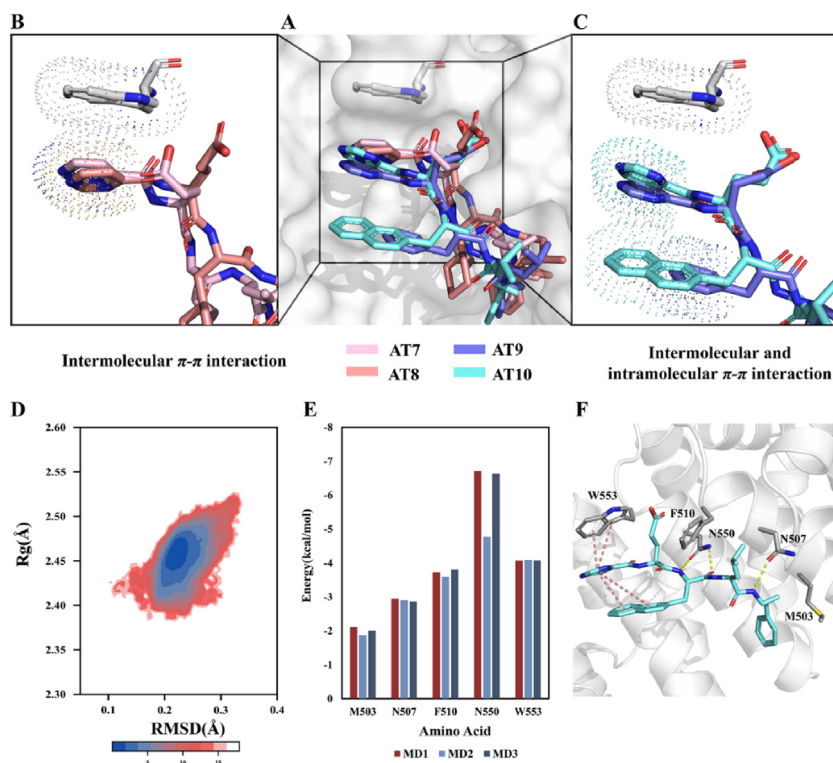
Compd.	R	IC <sub>50</sub> ± SD <sup>a</sup> (μmol/L)	Compd.	R	IC <sub>50</sub> ± SD <sup>a</sup> (μmol/L)
AT7		61.3 ± 7.2	AT9		95.4 ± 7.5
AT8		168 ± 9.5	AT10		9.34 ± 0.55

<sup>a</sup>The inhibitory potencies of the compounds were tested by the fluorescence-polarization (FP) competition assay. Values are means ± standard deviations (SD) of three independent experiments.

cyclohexyl (AT8), and phenyl (AT9) (Table 2). The partial loss of potency may result from the original intramolecular hydrogen bond breaking. Interestingly, AT10 (IC<sub>50</sub> = 9.3 μmol/L), with a larger naphthyl substituent, exhibited a 2-fold increase in potency over AT6.

To uncover the binding mode for the inhibitors complexed with APC, we next performed molecular docking with the aforementioned compounds (AT7–AT10). Guided by the reported

heptapeptide–APC complex (PDB: 5IZ6), the four inhibitors were docked to the binding pocket of APC. As shown in Fig. 2A, no significant difference was observed in the backbones of these molecules. However, the orientation of the modified groups at the S184 site in each inhibitor was quite different. Molecular docking results indicated that the position of aromatic groups tended to twist toward the N-terminus, which differed from the aliphatic functional groups (Fig. 2B and C). Importantly, the π-electron



**Figure 2** Molecular docking and MD simulation indicate  $\pi$ - $\pi$  interactions in binding. (A) Molecular docking results of AT7–10; (B) AT7 and AT8 included only intermolecular  $\pi$ - $\pi$  interactions. (Colored by light pink and salmon, respectively); (C) AT9 and AT10 included both intermolecular and intramolecular  $\pi$ - $\pi$  interactions (colored by slate and pale cyan, respectively); (D) Free energy landscape of MD simulations; (E) Key residues contributing to binding affinity larger than 2 kcal/mol; (F) Representative structure with key residues from the dominant cluster obtained from MD simulations.

cloud of naphthyl more easily formed intramolecular  $\pi$ - $\pi$  stacking interactions with the N-terminal pyrimidine ring *via* its favorable geometrical position. Therefore, we hypothesized that the higher inhibitory activity of AT10 resulted from an interesting sandwich-like two-layer  $\pi$ - $\pi$  stacking conformation, which was formed by W553, a pyrimidine cap, and naphthyl.

To verify our hypothesis, three 100 ns molecular dynamics (MD) simulations were performed on the AT10–APC complex according to the docking results. The calculations of the free energy landscape (FEL) revealed that the representative structure from the dominant cluster obtained from MD simulations was located at a single potential well (Fig. 2D). This result suggested that the conformation with two-layer  $\pi$ - $\pi$  stacking was sufficiently stable for binding. Furthermore, the critical residues that contributed considerably to binding affinity were identified according to MMPBSA calculations based on all MD trajectories of the AT10–APC system. Energy decomposition demonstrated that 5 residues, including M503, N507, F510, N550, and W553, contributed more than 2.0 kcal/mol to the binding affinity (Fig. 2E). Among these residues, N550 and N507 formed hydrogen bonds with the backbone of AT10. F510 and M503 exhibited hydrophobic interactions with AT10. These detected interactions corresponded with our findings in a previous heptapeptide–APC complex. More importantly, W553, which was not highlighted before, ranked second in energy contribution to binding affinity, indicating the key role of two-layer  $\pi$ - $\pi$  stacking in stabilizing the interaction between AT10 and APC (Fig. 2F). Considering MD simulations and experimental results, we

proposed that the stable two-layer  $\pi$ - $\pi$  stacking in novel inhibitors would be beneficial or even indispensable for the further optimization of compounds with better potency.

### 2.3. ONIOM model-driven N-terminal capping optimization for $\pi$ - $\pi$ stacking

To obtain inhibitors with higher potency against the APC–Asef interaction, we carried out a second round of optimizations for the N-terminal cap based on highlighted two-layer  $\pi$ - $\pi$  stacking. Since AT7–AT10 possess very similar molecular backbones, the aforementioned key residues, including N503, N507, F510 and N550, correspondingly exhibited little difference in their interactions with the ligands. In addition, considering the results of molecular docking, MD simulations, and energy decomposition, we realized that the N-terminal capping fragment played an essential role in improving binding affinity. The fragment stabilized the ligand in the bound state through the upper and lower  $\pi$ - $\pi$  stacking interactions. Therefore, we replaced diverse N-terminal functional groups to investigate the effect of  $\pi$ - $\pi$  stacking on molecular design.

Herein, we aimed to combine a computational model with bioactivity data *in vitro* to explore inhibitors with high potency. As shown in Supporting Information Table S1 and Fig. S1, we synthesized and evaluated a panel of inhibitors with various aliphatic and aromatic groups at the N-terminus (AT11–AT29). Considering the hydrophobic effect, electronic effect, and specific halogen atoms of substituents, different five- or six-membered

ring functional groups were introduced into the N-terminal cap. To explore the relationship between the two-layer  $\pi$ - $\pi$  stacking interaction and inhibitory activity, ONIOM computational models were constructed by replacing the pyrimidine ring in AT10 (Fig. 3A). After each model was optimized, three fragments of each optimized structure were selected for symmetry-adapted perturbation theory (SAPT) calculations, including the side chain of W553 (W), the N-terminal modification (R1), and the naphthyl modification (R2). Herein, SAPT calculations were performed to explore the properties of  $\pi$ - $\pi$  interactions in both the W-R1 group and R1-R2 group. The interaction in each group was composed of electrostatics, exchange, induction, dispersion, and total interaction. Although each single feature was not directly relevant to  $IC_{50}$ , the combined features saved and reflected certain information on the relationship between  $IC_{50}$  and  $\pi$ - $\pi$  stacking. Through forward subset selection, the exchange and induction in the W-R1 group (simplified as W-R1<sub>Ex</sub>, W-R1<sub>Ind</sub>), the exchange and induction in the R1-R2 group (simplified as R1-R2<sub>Ex</sub>, R1-R2<sub>Ind</sub>), and the number of heavy atoms after standardization (simplified as  $N_{\text{atom}}$ ) were chosen as features to build a multilinear regression model for predicting the  $pIC_{50}$  as Eq. (1):

$$pIC_{50} = -\text{Log} [IC_{50} (\mu\text{mol/L}) \times 10^{-6}] \quad (1)$$

Using AT7-AT29 data (training set), we obtained Eq. (2):

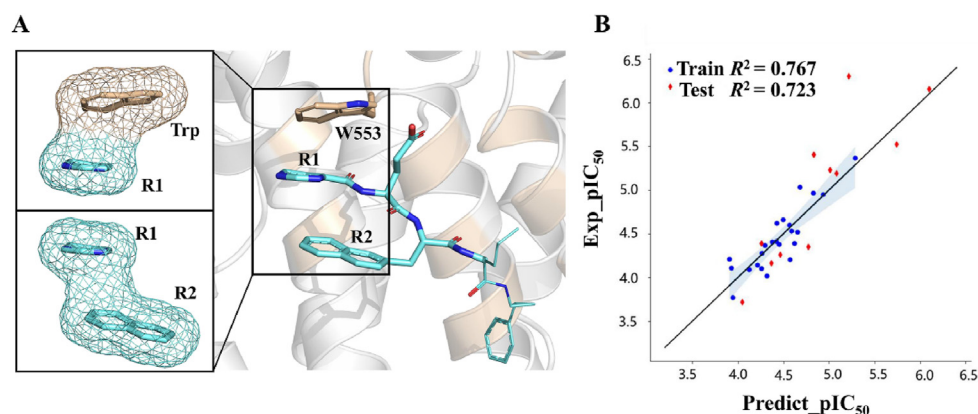
$$\begin{aligned} \text{predict\_}pIC_{50} = & 4.5269 + 0.2438 \times N_{\text{atom}} - 0.1830 \times (\text{W-R1}_{\text{Ex}}) \\ & - 1.5264 \times (\text{W-R1}_{\text{Ind}}) + 0.2560 \times (\text{R1-R2}_{\text{Ex}}) + \\ & 2.4377 \times (\text{R1-R2}_{\text{Ind}}) \end{aligned} \quad (2)$$

Based on the model with  $R^2 = 0.767$ ,  $\text{std} = 0.176$ , our selected features could explain the relationship between the properties of  $\pi$ - $\pi$  stacking and  $pIC_{50}$  (Fig. 3B). To test the model and obtain better inhibitors, we designed other N-terminal-modified inhibitors (test set, AT30-AT40, Table 3 and Supporting Information Fig. S2). Following the previous workflow, we predicted the theoretical  $pIC_{50}$  value of inhibitors in the test set by the regression model, which was 3.72, 5.23, 4.39, 4.26, 4.35, 5.19, 5.52, 5.41, 6.15, 4.16, and 6.30. In comparison, the FP assay showed that the experimental  $pIC_{50}$  values of AT30-AT40 were 4.04, 5.01, 4.26, 4.46, 4.77, 5.08, 5.74, 4.83, 6.09, 4.36, and 5.21. This result indicated that the values of

the  $IC_{50}$  predictions were approximately consistent with the experimental results. In particular,  $R^2$  in the test data set is 0.723, which illustrated that our computational model designed to predict inhibition was beneficial for molecular optimizations performed in the same pharmaceutical skeleton involving  $\pi$ - $\pi$  stacking interactions.

#### 2.4. Characterization of inhibitors complexed with APC

To explore the molecular basis for the increased inhibitory activity against the APC-Asef interaction, we determined the crystal structure of AT38 bound to APC with a resolution of 2.10 Å. The structure illustrated an accurate distribution of the electron cloud for AT38 in the APC-ARM pocket (Fig. 4A and B). Data collection and refinement details for the crystal structure are presented in Supporting Information Table S2. The structure showed that AT38 occupied the large hydrophobic APC-ARM pocket and extended around F510 in a U-shaped conformation (Fig. 4C). As expected, the N-terminal pyrimidine moiety in AT38 was involved in unique two-layer  $\pi$ - $\pi$  stacking interactions, which included a typical intermolecular interaction with W553 of APC (distance = 4.0 Å) and an intramolecular interaction with the introduced naphthyl (distance = 3.9 Å). Moreover, the critical salt bridge was maintained between E183 and K516. We have tried to replace Glu with Asp to diminish the chain length for carbon atom, while the inhibitory activity of compound AT41 was significantly decreased (Table 4). This further demonstrates the importance of Glu for maintaining the inhibition efficiency. In addition, a six-membered intramolecular hydrogen bond tended to form, which involved two water molecules, the carboxyl of E183 and the nitrogen atom of the amine (Supporting Information Fig. S3). The steric constraint of the six-membered hydrogen bond was significant for increasing binding affinity. In addition to strong hydrogen bonds generated by the backbone and surrounding residues, beneficial hydrophobic interactions around L185 were consistent in our leading MAI-400. The structure also showed that the C-terminal capping substituent stretched through the optimized cyclopropane to interact with M503 and V543 (Fig. 4D). The rigid linker assisted in restraining the orientation of benzyl to form positive hydrophobic interactions.



**Figure 3** Computer-aided N-terminal capping optimization for  $\pi$ - $\pi$  stacking. (A) ONIOM computational model for symmetry-adapted perturbation theory (SAPT) calculations. Substrate (colored by pale cyan) and residues approximately 4 Å (colored by wheat). Atoms shown in sticks were included in the high layer in the ONIOM calculations, and the left in lines or cartoons were in the low layer. W-R1 and R1-R2 groups were selected to calculate SAPT; (B) The regression model for predicted  $pIC_{50}$  and experimental  $pIC_{50}$ .

**Table 3** Analysis of the ONIOM model for the test set.

Compd.	R1	R2	Trp–R1				R1–R2				N <sub>atom</sub> <sup>c</sup>	IC <sub>50</sub> <sup>f</sup>	pIC <sub>50</sub>
			Ele. <sup>a</sup>	Exc. <sup>b</sup>	Ind. <sup>c</sup>	Dis. <sup>d</sup>	Ele.	Exc.	Ind.	Dis.			
AT30			-3.24	8.03	-0.97	-7.28	-3.80	7.98	-1.02	-5.71	50	190	3.72
AT31			-10.4	16.8	-2.02	-13.9	-3.31	6.01	-0.63	-6.12	55	5.94	5.23
AT32			-2.78	9.65	-1.10	-10.1	-2.18	6.25	-0.75	-6.50	51	40.6	4.39
AT33			-6.11	15.8	-1.76	-14.7	-3.70	8.73	-0.87	-0.87	52	54.9	4.26
AT34			-4.83	12.9	-1.65	-12.1	-2.68	7.16	-0.69	-7.12	50	44.6	4.35
AT35			-8.57	18.7	-2.58	-15.6	-5.75	11.8	-1.25	-10.5	51	6.45	5.19
AT36			-10.8	17.9	-2.89	-14.4	-4.97	10.4	-1.09	-9.46	51	3.05	5.52
AT37			-8.13	17.2	-1.97	-14.1	-4.86	11.2	-1.07	-10.7	52	3.93	5.41
AT38			-7.31	16.6	-2.41	-15.2	-4.95	11.2	-1.15	-11.0	52	0.67	6.15
AT39			-5.82	13.5	-1.77	-12.7	-4.46	10.3	-0.99	-9.75	52	68.8	4.16
AT40			-9.69	19.2	-2.63	-15.8	-4.95	11.2	-1.15	-11.0	52	0.50	6.30

<sup>a</sup>Ele. means electrostatics (kcal/mol).<sup>b</sup>Exc. means exchange (kcal/mol).<sup>c</sup>Ind. means induction (kcal/mol).<sup>d</sup>Dis. means dispersion (kcal/mol).<sup>e</sup>N<sub>atom</sub> means the number of heavy atoms.<sup>f</sup>Values are means of three independent experiments, and the data of corresponding standard deviation (SD) are shown in CSV in the supplementary information.

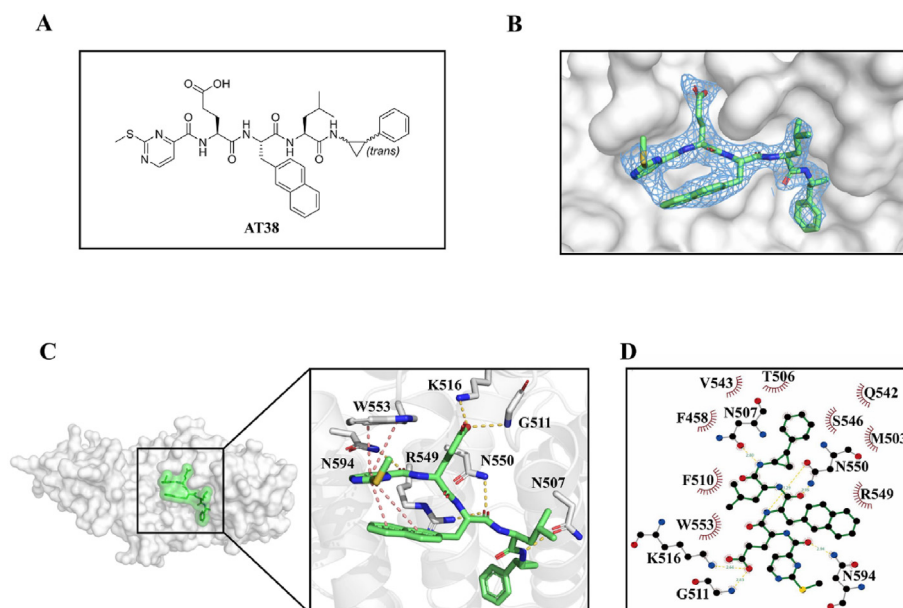
Given that the configurations of central naphthyl in the inhibitors exert a certain influence on  $\pi$ – $\pi$  interactions, we subsequently synthesized the negative control compounds AT42 (IC<sub>50</sub> = 33  $\mu$ mol/L) and AT43 (IC<sub>50</sub> = 127  $\mu$ mol/L) containing D-naphthyl (Table 4). As expected, the potency was significantly decreased. In addition, considering that the position for C-terminal modification is sensitive to the inhibitory activity of the inhibitors, we performed configuration resolution to synthesize inhibitors AT44 and AT45 with single-configuration (*R,S*) or (*S,R*). The C-terminal fragment with (*R,S*) was more beneficial for stabilizing the inhibitor. Consequently, the best inhibitor, AT46, was generated with an IC<sub>50</sub> of 0.11  $\mu$ mol/L.

To further investigate the binding affinity of designed inhibitors for APC, we determined the binding kinetics of AT6 by Isothermal Titration Calorimetry (ITC) and Surface Plasmon Resonance (SPR). The ITC results showed that AT6 directly interacted with APC with a  $K_d$  value of 38.3  $\mu$ mol/L (Fig. 5A). Moreover, SPR experiments confirmed that AT6 and AT46 reversibly interacted with APC in a dose-dependent manner (Fig. 5B and C). It exhibited fast binding and slow dissociation characteristics with a simple 1:1 Langmuir binding fit model. The equilibrium dissociation constant values ( $K_d$ ) were 23.7  $\mu$ mol/L for AT6 and 0.23  $\mu$ mol/L for AT46, which corresponded with the convergence of the FP and ITC assays. Particularly, we also carried out similar studies on other representative compounds (AT7, AT9, AT10, AT38, AT40 and AT44) as shown in Supporting

Information Fig. S4 and Table S3. These results indicated that the SAR based on the binding affinities presented a good correlation of IC<sub>50</sub> values determined by FP.

### 2.5. AT47 inhibited SW480 cells migration

To determine if the inhibitor disrupts the APC–Asef interaction in cells, we first selected AT46 and performed a coimmunoprecipitation (Co-IP) study in drug-treated cell lysates. HEK293T cells were transiently transfected with FLAG-tagged APC (303–876) and hemagglutinin (HA)-tagged Asef (170–632) plasmids. The cell lysates were harvested 48 h after transfection and treated with DMSO, MAI-400 (5  $\mu$ mol/L), MAI-203 (5  $\mu$ mol/L), or AT46 (0.2, 1 or 5  $\mu$ mol/L) for 2 h. MAI-203 (<sup>181</sup>AGEA(CP)<sup>185</sup>YE<sup>187</sup>, IC<sub>50</sub> = 2.16  $\pm$  0.17  $\mu$ mol/L) was used as a positive control. Then, the drug-treated lysates were incubated with anti-FLAG<sup>®</sup> M2 affinity gel overnight. We observed that AT46, which is comparable to MAI-400, dose-dependently attenuated the APC–Asef interaction in cell lysates more effectively than MAI-203 (Fig. 6A). In an effort to further elucidate the APC–Asef disruption by inhibitors, we then performed the Co-IP assay for 10 compounds including key SAR representatives shown in Tables 3 and 4. As expected, the results demonstrated the inhibitors apparently disrupted the APC–Asef interaction in cell lysates, which corresponded with the IC<sub>50</sub> values of the FP assays (Supporting Information Fig. S5).



**Figure 4** X-ray cocrystal structure of AT38 complexed with APC (PDB code 8GSJ). (A) The chemical structure of compound AT38. (B) Electron-density map for AT38 bound in the APC-ARM. APC is shown as a solvent-accessible surface (gray), and AT38 is depicted by sticks (lime carbon atoms). The electron density map is shown as a blue mesh. (C) Overview of binding interactions between AT38 (lime carbon atoms and green surface) and APC (white surface and gray key residues atoms). The yellow dashed lines represent hydrogen bonds, the salmon dashed lines represent  $\pi-\pi$  stacking interactions. (D) Interactions of AT38 with surrounding residues (including strong hydrogen bonds and hydrophobic interactions) revealed by the crystal structure.

**Table 4** Inhibitory activity of compounds AT41–46 targeting APC–Asef.

Compd.	Structure	IC <sub>50</sub> ± SD <sup>a</sup> (μmol/L)
AT41		19.3 ± 0.58
AT42		33.1 ± 3.1
AT43		127 ± 6.6
AT44		0.480 ± 0.070
AT45		8.61 ± 0.12
AT46		0.110 ± 0.0030

<sup>a</sup>Values are means ± standard deviations (SD) of three independent experiments.



Since it was difficult for the previously reported MAI inhibitors to penetrate the cell membrane, TAT peptides were needed to achieve the inhibitory potencies<sup>18–20</sup>. We hypothesized that this might result from the presence of glutamate carboxyl groups that hindered the entry of peptides into the cell membrane. Therefore, as shown in Fig. 6B, we tried to enclose the carboxyl group into an ester and synthesized AT47 (inhibition rate 24.4% at 400  $\mu\text{mol/L}$ ). The compound AT47 was designed as a prodrug derivative of AT46 with a *tert*-butyl protector for cellular level experiments. We next performed Co-IP of exogenous HA-APC (303–876) and FLAG-Asef (170–632) in HEK293T cells treated with AT47, AT46, and MAIT-203 at a concentration of 20  $\mu\text{mol/L}$  for 48 h. Notably, MAIT-203 ( $\text{IC}_{50} = 18.0 \pm 0.56 \mu\text{mol/L}$ ) was the peptidomimetic of MAI-203 conjugated TAT peptide, which was used as the control. Although AT46 effectively inhibited the APC–Asef interaction in the cell lysate, the results suggested that AT46 caused no disrupting effect on the APC–Asef interaction in the cell model. Similar to MAIT-203, novel inhibitor AT47 notably diminished APC–Asef PPI, which improved the cell membrane permeability of AT46 with *tert*-butyl protection (Fig. 6C). These results further demonstrated that the inhibitor could efficiently disrupt the APC–Asef PPI in cells without TAT support.

To investigate the effect of AT47 on the migration of CRC cells mediated by the APC–Asef interaction, we conducted a subsequent wound healing assay. After SW480 cells were treated with compounds for 48 h, the results showed that AT47 inhibited the migration of SW480 cells at 20  $\mu\text{mol/L}$ , which was comparable to the inhibitory effect of MAIT-203 (Fig. 6D and E). Similarly, in a 72 h Transwell-based migration assay, AT47 suppressed the migration of SW480 cells at 20  $\mu\text{mol/L}$  compared to DMSO and MAIT-203 (Fig. 6F and G). Furthermore, we discovered that the parent molecule AT46 exhibited no inhibition in the wound healing or Transwell assay, whereas the prodrug derivative AT47 significantly inhibited the SW480 cell migration, which was consistent with the Co-IP results described above. These data further revealed that AT47 with *tert*-butyl protection improved permeability to cross the cell membrane to some extent. We also evaluated the toxic effects of AT47 and AT46 on the proliferative viability of SW480 cells expressing truncated APC using the CCK-8 assay. The results showed that AT47, AT46 and MAIT-203 did not damage the survival ability of SW480 cells at a concentration of 20  $\mu\text{mol/L}$  (Fig. 6H). Overall, these data illustrated that novel inhibitor AT47 exhibited

anti-migration ability and low cytotoxicity for colorectal cells expressing truncated APC.

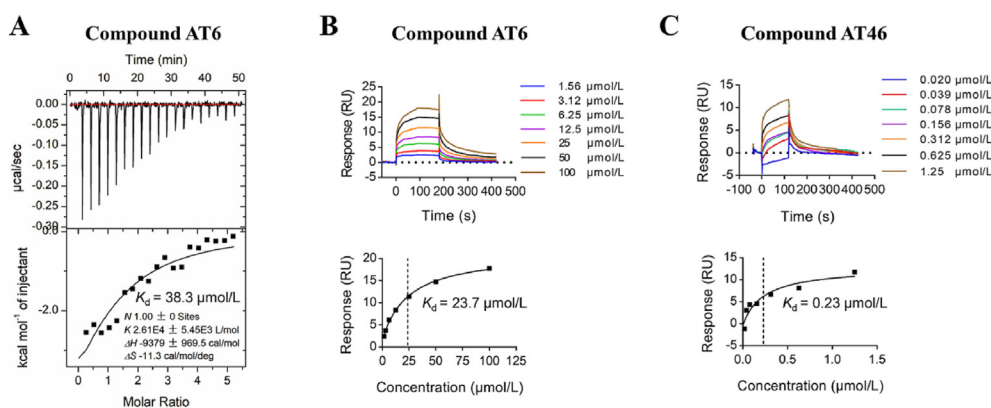
### 2.6. AT47 inhibited lung metastasis of colorectal cancer *in vivo*

To explore the therapeutic potential of inhibitors for mCRC, we attempted to evaluate the effect of compound AT47 on tumor metastasis *in vivo*. Encouraged by the excellent *in vitro* efficacy, we first studied the pharmacokinetics of inhibitors in male BALB/c mice. As shown in Fig. 7A and Table 5, compounds AT46 and AT47 exhibited a significant improvement *in vivo* half-life compared to MAI-203. This further suggested that structural-guided optimization improved both potency and metabolic stability of inhibitors, providing the potential druggability superior to reported peptides. Next, we investigated the efficacy of compound AT47 in the lung metastasis mouse model for CRC. The mouse model of lung metastasis was established by tail-vein injection of SW480 cells into the BALB/c nude mice. After the intraperitoneal administration for 2 weeks, a reduction in lung metastatic nodules was observed in the group treated with compound AT47 (2 mg/kg) (Fig. 7B). This indicates that inhibitor AT47 holds promise in the suppression of colorectal cancer metastasis *in vivo* by disrupting the interaction between APC and Asef.

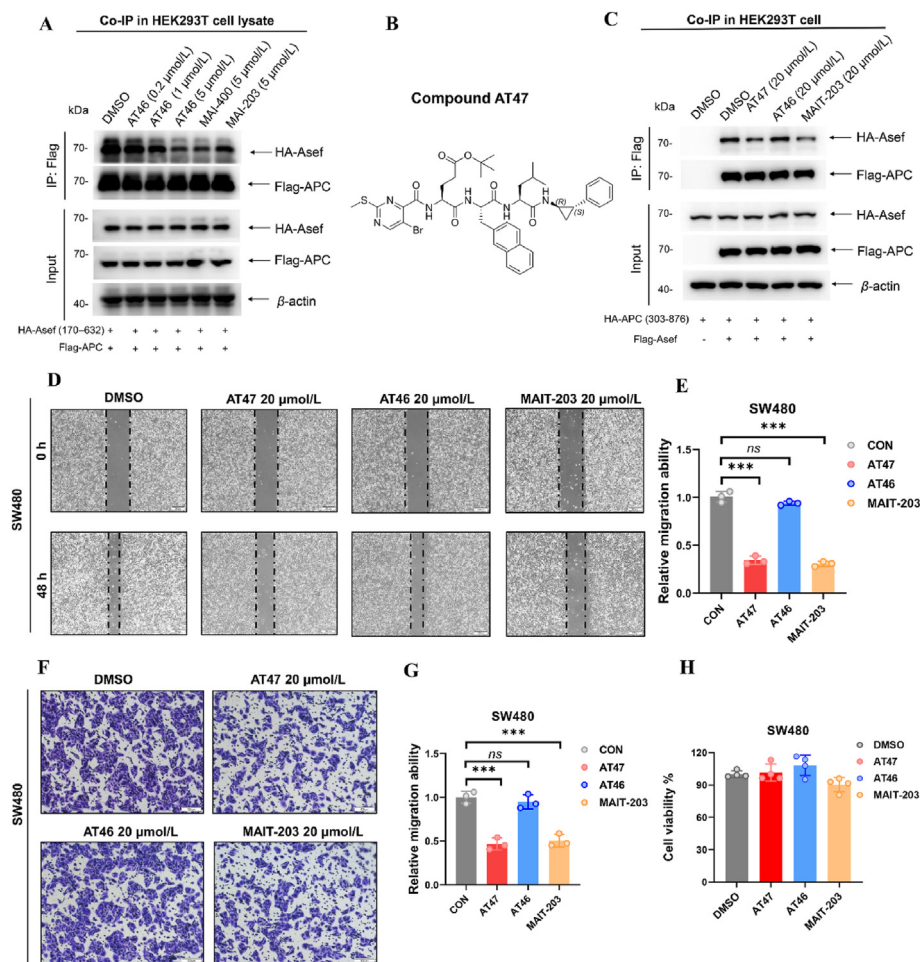
Taken together, the results indicated that a series of novel inhibitors targeting APC–Asef were developed with the integration of chemical modifications and ONIOM model-driven optimizations. In addition, experimental evaluations were performed to improve the inhibitor potency. The results illustrated that the best inhibitor, AT46, exhibited excellent potency (24-fold) over the parental MAI-400. Furthermore, its derivative AT47 demonstrated the pronounced anti-migration effects of colorectal cancer *in vivo*. Importantly, this work provides a rational design strategy that combines structure-based modification with computer-driven optimization to improve the potency of APC–Asef inhibitors, which will facilitate the development of drug-like molecules in the future.

## 3. Conclusions

Concerted efforts have been dedicated to identifying drug-like molecules against the APC–Asef interaction, which is a well-established target for mCRC therapy. However, discovering and developing inhibitors with high specificity, great potency, and metabolic stability remains a challenging endeavor<sup>40–43</sup>. Based on the cocrystal structure of MAI-400 complexed with



**Figure 5** Binding affinity for compounds AT6 and AT46 by ITC and SPR. (A) ITC titration curves of AT6. (B–C) Representative SPR sensorgrams and plot of the response signals at equilibrium against the concentrations of AT6 (B) and AT46 (C) binding to APC.

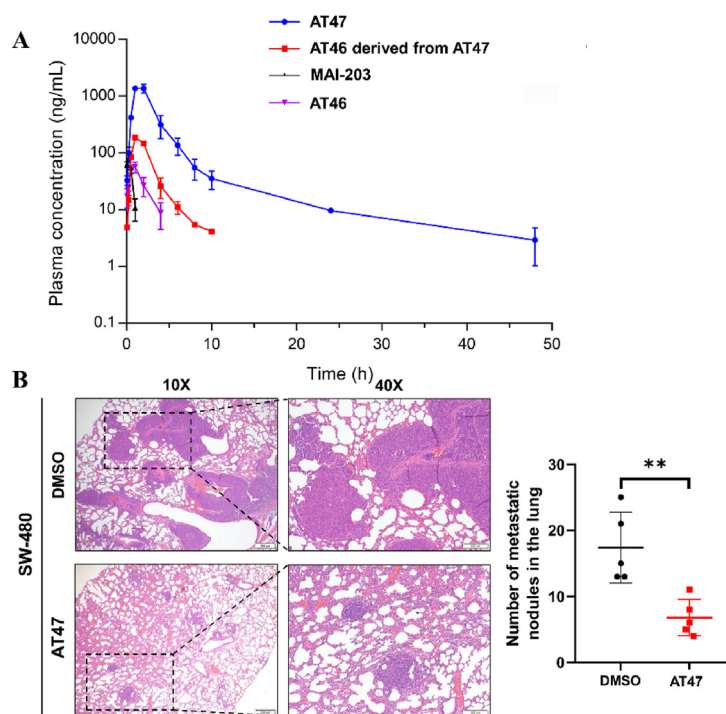


**Figure 6** The compound AT47 suppresses APC–Asef-mediated CRC cells migration. (A) Co-IP in HEK293T cell lysates transfected with Flag-APC (303–876) and HA-Asef (170–632) and treated with DMSO, AT46 (0.2, 1 and 5 μmol/L), MAI-400 (5 μmol/L) and MAI-203 (5 μmol/L) for 24 h. (B) The chemical structure of compound AT47. (C) Co-IP of exogenous HA-APC (303–876) and Flag-Asef (170–632) in HEK293T cells treated with DMSO, AT47 (20 μmol/L), AT46 (20 μmol/L) and MAIT-203 (20 μmol/L) for 48 h. (D) The wound healing results of SW480 cells treated with DMSO, AT47 (20 μmol/L), AT46 (20 μmol/L) and MAIT-203 (20 μmol/L) for 48 h. Representative images scale bar: 200 μm. (E) Quantitative cell migration data are expressed relative to the migration ability of the DMSO-treated group. Data are represented as the mean ± SD ( $n = 3$  independent experiments). (F) The Transwell-based migration results of SW480 cells treated with DMSO, AT47 (20 μmol/L), AT46 (20 μmol/L) and MAIT-203 (20 μmol/L) for 72 h. Scale bar: 100 μm. (G) The number of cells that migrated was normalized to the average cell count of DMSO-treated cells. Data are shown as the mean ± SD ( $n = 3$  independent experiments). (H) The proliferation results of SW480 cells treated with DMSO, AT47 (20 μmol/L), AT46 (20 μmol/L) and MAIT-203 (20 μmol/L) for 48 h  $***P < 0.001$ , ns means not significant.

APC, we designed and synthesized a series of novel inhibitors by employing molecular modification and computer-driven optimizations. Through detailed X-ray structural characterization and inhibitory activity assays, AT46 was determined to be a novel inhibitor that targets the APC–Asef interface; compared to parental compound MAI-400, AT46 exhibited a 24-fold increase in potency.

A critical sandwich-like two layers of  $\pi$ - $\pi$  stacking interactions, including intermolecular and intramolecular interactions, were uncovered and verified in the crystal structure of AT38 complexed with APC; this structure contained W553 of APC, a N-terminal cap, and side-chain naphthyl, which significantly improved the inhibitory activity of APC. Notably,  $\pi$ - $\pi$  interactions function as a particular type of van der Waals force from noncovalent weak interactions. Considerable efforts have

been dedicated to the role of  $\pi$ - $\pi$  stacking in the stability of protein folding, but few studies have addressed its definite application in rational drug design<sup>44–48</sup>. In this study, we investigated the effect of  $\pi$ - $\pi$  stacking on binding affinity in the process of computer-aided N-terminal capping modification. The typical SAPT method was exploited to calculate the noncovalent interactions and reveal the fundamentals of the interaction pattern between two layers of the structural segment, and *in vitro* biochemical evaluations were combined to characterize the efficient inhibition. Through these efforts, we developed a new class of inhibitors superior to MAI-400 (Supporting Information Fig. S6). Collectively, introducing  $\pi$ - $\pi$  stacking in peptidomimetic optimization provides a breakthrough in the constraints of backbone conformation, which provides an alternative approach to promote binding affinity.



**Figure 7** AT47 inhibits the lung metastasis in mCRC mouse model. (A) The plasma concentration-time curves of compounds AT46, AT47 and MAI-203 in BALB/c mice after 1 mg/kg intraperitoneal administration ( $n = 3/\text{group}$ ). The red line represents AT46 derived from AT47 *in vivo*. (B) AT47 inhibits the lung metastasis of CRC cells in mouse models. The lung metastatic CRC model was established by tail vein injection of SW480 cells in BALB/c nude mice ( $n = 5/\text{group}$ ). Lung sections were subjected to H&E staining (left). The number of metastatic nodules in the lung specimens was analyzed.  $**P < 0.01$  (right).

**Table 5** Pharmacokinetic parameters of compounds AT46–47 and MAI-203 in BALB/c mice ( $n = 3$ ).

PK parameter	AT46	AT47	AT46 derived from AT47	MAI-203
$t_{1/2}$ (h)	$1.20 \pm 0.50$	$11.8 \pm 5.7$	$1.36 \pm 0.31$	$0.24 \pm 0.06$
$T_{\max}$ (h)	$0.83 \pm 0.29$	$1.67 \pm 0.58$	$1.00 \pm 0.00$	$0.25 \pm 0.00$
$C_{\max}$ (ng/mL)	$60.8 \pm 5.65$	$1457 \pm 119$	$188 \pm 16.3$	$101 \pm 25.0$
$AUC_{\text{last}}$ (h·ng/mL)	$124 \pm 18.4$	$4803 \pm 868$	$480 \pm 63.2$	$52.4 \pm 6.07$
MRT (h)	$1.96 \pm 0.58$	$4.97 \pm 1.49$	$2.26 \pm 0.30$	$0.43 \pm 0.07$

Bioactive peptides typically suffer from a short half-life and rapid plasma clearance, which limit their potential application in clinical practice. To overcome these intrinsic deficiencies, several inhibitors were obtained by manipulating unnatural amino acids and modifying the terminal capping structures of the original scaffold<sup>49–54</sup>. Herein, we utilized the same strategy to obtain several inhibitors with the improved human plasma stability (Supporting Information Table S4). We also carried out a preliminary exploration to improve membrane permeability based on AT46. This involved enclosing the carboxyl group of Glu with *tert*-butyl ester, and the expected results were achieved. Nevertheless, the molecular diversity should be further expanded based on the peptidomimetic scaffold. More efforts are needed to investigate the molecular mechanism of cell membrane permeation. In addition, backbone cyclization may serve as an alternative approach to improve the drug-like properties of peptides without damaging functionally relevant side chains.

In summary, we designed and synthesized a series of novel inhibitors targeting the APC–Asef interaction. Structure-based modification and computer-driven optimization provided the best

tripeptide inhibitor, AT46, with an  $IC_{50}$  of 110 nmol/L. The X-ray crystal structure revealed that the improvement in compounds potencies was achieved when the inter- and intramolecular  $\pi$ – $\pi$  stacking interactions were mediated. Importantly, the inhibitor AT47 was demonstrated to be effective in inhibiting mCRC *in vivo* mediated by the APC–Asef interaction. The potency, stability and membrane permeability of optimized inhibitors were superior to those of the parental compound MAI-400. In summary, this study involved an application of structure-based and computer-driven rational design for inhibitor optimization, which elucidated the further development of desirable drug-like molecules targeting the APC–Asef interaction.

## 4. Experimental

### 4.1. Synthesis and characterization of the target compounds

Experimental details of the synthetic works were included in the Supporting Information.

#### 4.2. FP-based competition assays

The recombinant protein APC (303–739) was diluted in FP buffer (50 mmol/L HEPES, pH 7.5, 300 mmol/L NaCl, 1 mmol/L EDTA, 1 mmol/L DTT) to make a working solution at 27.4 nmol/L. The diluted APC protein (91  $\mu$ L) was combined with a 2-fold serial dilution of peptidomimetics (4  $\mu$ L) and incubated at room temperature for 1 h, followed by the addition of 5  $\mu$ L of 400 nmol/L FITC-labeled peptide (Cbz-AGESLYEK-FITC-NH<sub>2</sub>). The FP signals were measured in 96-well microplates (3650, Corning) after 1.5 h of incubation at room temperature using a Synergy neo microplate reader (BioTek Instruments, Inc.). Positive (free tracer only) and negative (protein/tracer complex only) controls were included on each plate. All experiments were performed in triplicate. The dose-response curves were fitted by nonlinear regression analysis using GraphPad Prism 7.0 software. The IC<sub>50</sub> values of peptides were calculated as the mean of three independent experiments.

#### 4.3. Molecular docking, MD simulations, and binding free energy calculations

The structure of APC (PDB ID: 4YJE) was selected from the PDB data bank for molecular docking since 4YJE has the most complete structural information in all reported crystals. In addition, as the cocrystal structure with APC and heptapeptide inhibitor, 5IZ6 was utilized to guide our docking experiments. Referring to the position and size of the ESL sequence in 5IZ6, AT7–10 were docked to APC (4YJE) by AutoDock4.2.6. All 50 docking results were clustered and ranked by docking scores, and the single docking pose with the best energy score in the most clusters was selected.

The docking results of AT10 were utilized to perform molecular dynamics (MD) simulations to determine its best inhibitory ability through the Amber18 software package with the ff14SB forcefield. The complex is solvated to a box of TIP3P water. To achieve system charge neutralization, one molecule of sodium ion was added. To prevent inappropriate atomic collisions, we performed a two-step minimization process for the system as follows: the first step was performed for all water molecules, and the second step was performed to prevent the remaining parts from colliding inappropriately. Then, we progressively heated the system from 0 to 300 K in 100 ps. After heating the system, we switched it to constant pressure and temperature mode (NPT). In this mode, we performed a 200 ps equilibration to ensure that the system was at the correct density. Finally, we took the last frame of the NPT process as the initial structure to run three parallel 100 ns trajectories for further analysis. The particle mesh Ewald (PME) method and SHAKE algorithm were both introduced for long-range electrostatic interactions and fixing bonds and angles involving hydrogen atoms, respectively. The cutoff of van der Waals interactions was set to 10.0 Å.

The binding free energies between tripeptide and APC were estimated *via* the molecular mechanics Poisson–Boltzmann surface area (MM-PBSA) through the python program MMPBSA.py implemented in AMBER 18. MM-PBSA is an efficient post-processing end-state method for binding free energy calculations utilizing the free energies of the entire complex, the ligand, and the receptor. The binding free energy for a ligand–receptor complex system is represented as the energy difference between the free energy of the total complex and that of the ligand and receptor.

Due to the typical instability observed in the initial stages of MD simulations, frames from the first 20 ns of each of the three parallel trajectories were excluded during the binding free energy calculations. In MM/PBSA calculations, 400 frames were sampled from each trajectory at intervals of 100 frames, and three parallel trajectories were employed for each system. Other parameters are all default. Additionally, our primary objective was to identify pivotal residues that play a significant role in stabilizing the tripeptide. The computed free energies were decomposed into specific residue contributions using a per-residue decomposition scheme. Key residues (energy contribution  $\geq 2.0$  kcal/mol) and relevant interactions were found.

#### 4.4. QM/MM and symmetry-adapted perturbation theory (SAPT) calculations

The original model of the QM/MM calculation was extracted as representative structures from the dominant clusters obtained from MD simulations when we selected residues within 4 Å of the tripeptide to build the ONIOM model. All QM/MM calculations were performed with the ONIOM (B3LYP-D3/6-31 g(d): Amber) method by Gaussian 16 Software, which was an excellent choice for optimizing systems involving weak interactions, especially pi–pi stacking. It not only provides reliable accuracy but also exhibits faster computational speed<sup>55</sup>. To focus on two-layer  $\pi$ – $\pi$  stacking, the side chain of W553, the N-terminal modification, the naphthyl (S184 site) modification, and ES<sup>184</sup> parts of the tripeptide were designated as the high layer, and the others were designated as the low layer. The interaction between QM and MM layers was treated with the electrostatic embedding formalism.

Symmetry-adapted perturbation theory (SAPT) is a typical method used to investigate the nature of noncovalent  $\pi$ – $\pi$  interactions, and the energy component analysis of this method can reveal various intermolecular force contributions, including induction (polarization), short-range exchange-repulsion, London dispersion, and electrostatics. For each optimized QM/MM structure, the interaction between the sidechain of W553 and the N-terminal cap, as well as the N-terminal cap and S184-site modification, were calculated with SAPT by PSI4 software. All input files for PSI4 software were generated by Multiwfn. Herein, the bronze standard of SAPT was sSAPT0/jun-cc-pVDZ.

#### 4.5. Crystallization and structure determination

The APC protein was expressed, purified, and crystallized as previously reported. AT38 has a purity of at least 95%. The APC protein including 407–751 residues (15 mg/mL) and AT38 with a final concentration of 2 mmol/L, as well as three kits (SM4, IHT, and VV), were combined in 96-well drop plates. Afterward, 0.5  $\mu$ L of the mixture combined with 0.5  $\mu$ L of the crystallization buffer in the sitting drop was equilibrated against a well of 50  $\mu$ L of the crystallization buffer at 18 °C. The crystal was cryoprotected in 0.2 mol/L ammonium sulfate, 0.1 mol/L Tris (pH 8.0), 25% (w/v) PEG 3350, and 15% glycerol before being flash-cooled in liquid nitrogen. Diffraction data were collected on beamline BL17U1 at 100 K in the Shanghai Synchrotron Radiation Facility. The crystal structure was determined, further refined, and deposited into the PDB with code 8GSJ.

#### 4.6. Isothermal titration calorimetry assay

ITC experiments were performed using a MicroCal ITC200 calorimeter (GE Healthcare). APC protein and AT6 were diluted with buffer containing 50 mmol/L HEPES pH 7.5, 300 mmol/L NaCl and 1 mmol/L EDTA. The final DMSO concentration was 2.5%. The cell was loaded with APC protein at 20  $\mu\text{mol/L}$ , and the syringe was filled with 500  $\mu\text{mol/L}$  AT6. The experiments were performed using an initial injection of 0.2  $\mu\text{L}$  followed by 19 injections of 2  $\mu\text{L}$  at 25 °C. The data were analyzed using a single-site binding model in MicroCal ITC200 analysis software to generate the enthalpy changes ( $\Delta H$ ), entropy changes ( $\Delta S$ ), and the association constant ( $K$ ) of binding with the stoichiometry ( $N$ ) fixed to 1. The changes in free energy ( $\Delta G$ ) were calculated as Eq. (3):

$$\Delta G = \Delta H - T \cdot \Delta S \quad (3)$$

#### 4.7. Surface plasmon resonance

SPR experiments were performed using a Biacore T200 system equipped with a CM5 sensor chip. The surface was activated with a 1:1 mixture of 0.1 mol/L NHS and 0.1 mol/L EDC at a flow rate of 10  $\mu\text{L}/\text{min}$ . His-tagged APC (303–739) at 10  $\mu\text{L}/\text{mL}$  in 10 mmol/L sodium acetate, pH 5.0, was immobilized on flow cell 2; flow cell 1 was left blank to serve as a reference surface. Both surfaces were blocked with 1 mol/L ethanolamine, pH 8.0. To collect the kinetic binding data, serial concentrations of AT6 in 1  $\times$  PBSP containing 10% DMSO, pH 7.4, were injected over the two flow cells at a flow rate of 30  $\mu\text{L}/\text{min}$  at 25 °C. The association and dissociation times were 180 and 300 s, respectively. The experiments were performed in triplicate. The corresponding sensorgrams were corrected for the DMSO bulk response by using calibration curves obtained with a 9%–10% DMSO running buffer. The data were fitted to an affinity model in Biacore evaluation software.

#### 4.8. Coimmunoprecipitation

For the exogenous co-IP of APC–Asef in drug-treated cell lysates, HEK293T cells were plated in six-well plates on Day 1 and transfected with pBabe puro FLAG-APC (303–876) and pBabe puro HA-Asef (170–632) by Neofect DNA transfection reagent (Neofect) on Day 2. Forty-eight hours after transfection, the cells were washed twice with cold PBS and lysed in NP-40 lysis buffer supplemented with protease inhibitor cocktails (ApexBio, K1007) for 1 h on ice. The cell lysates were clarified by centrifugation at 20,000  $\times g$  at 4 °C for 10 min. The supernatant was incubated with DMSO, MAI-400 (5  $\mu\text{mol/L}$ ), MAI-203 (5  $\mu\text{mol/L}$ ), or AT46 (0.2, 1 or 5  $\mu\text{mol/L}$ ) for 2 h at 4 °C. Then, 30  $\mu\text{L}$  of anti-FLAG M2 Affinity Gel (Sigma Aldrich, A2220) was added and incubated overnight at 4 °C on a vertical rotator. The next day, the samples were centrifuged (7000  $\times g$  for 30 s at 4 °C), and the supernatant was discarded. The beads were washed four times with NP-40 lysis buffer, and the bound proteins were eluted in SDS sample buffer for immunoblotting analysis and detected with anti-FLAG (Sigma; F1804, 1:1000), anti-HA antibody (Sigma; H9658, 1:20,000) and goat anti-mouse IgG secondary antibody (Signalway antibody; L3032, 1:25,000).

For exogenous immunoprecipitation at the cellular level, cells were harvested in NP-40 lysis buffer (0.3% NP-40, 50 mmol/L

Tris-HCl at pH 7.5, 150 mmol/L NaCl, 1 mmol/L PMSF, 25 mmol/L NaF, 1 mmol/L  $\text{Na}_3\text{VO}_4$ ) supplemented with cOmplete™ Protease Inhibitor Cocktail (Roche). HEK293T cells were transfected with pcDNA-HA-APC (303–876) and pRK7-Flag-Asef, and the cells were incubated with different concentrations of DMSO/AT46/AT47/MAIT-203 for 48 h. Then, the cells were harvested in 0.3% NP-40 lysis buffer, and the cell lysate was incubated with anti-FLAG magnetic beads (Sigma) for 3 h at 4 °C. The precipitated protein was eluted from beads with 60  $\mu\text{L}$  1  $\times$  loading buffer after boiling for 10 min at 95 °C.

#### 4.9. Wound healing assay

A total of 1  $\times 10^6$  SW480 cells were seeded into 6-well plates and incubated at 37 °C and 5%  $\text{CO}_2$ . When the cell density was 100%, a scratch wound was formed in the cell monolayer. The medium was removed, and the cells were washed with 1  $\times$  PBS and then cultured in culture medium containing 1% FBS and AT47/AT46/MAIT-203. The corresponding photos were captured at the time of scratching and after 48 h.

#### 4.10. Transwell migration assay

Migration assays were performed using Transwell chambers in 24-well plates (Corning #3422). Cells were seeded in the upper chambers at a density of 1.5  $\times 10^5$  SW480 cells per well in 250  $\mu\text{L}$  of serum-free medium. The lower chambers were filled with 750  $\mu\text{L}$  of complete medium. AT47, AT46 and MAIT-203 were added to the upper and lower chambers. After 72 h, the Transwell inserts were washed twice with 1  $\times$  PBS. The top membrane was swiped with cotton swabs to remove the non-migrated cells, and the migrated cells were stained with crystal violet before the cell number was counted to evaluate the migration ability.

#### 4.11. Cell cytotoxicity assay

A total of 2000 cells were plated in a 96-well plate and treated with DMSO, AT47 (25  $\mu\text{mol/L}$ ), AT46 (25  $\mu\text{mol/L}$ ) and MAIT-203 (25  $\mu\text{mol/L}$ ) for 48 h. Cell viability was measured by the CCK-8 assay (Yeasen Biotechnology, Shanghai) according to the manufacturer's instructions.

#### 4.12. Pharmacokinetic study

The pharmacokinetic profile of AT46, AT47 and MAI-203 was investigated in Pharmaron inc. following single intraperitoneal administration in male BALB/c mice at 1 mg/kg 5 mL/kg formulated in DMSO: Cremophor EL: 10% HP- $\beta$ -CD in saline (2:8:90). Blood samples were collected from dorsal metatarsal vein at pre-dose (0 h), and 0.083, 0.25, 0.5, 1, 2, 4, 6, 8, 10, 24, 48 h post dose. Plasma samples were obtained by centrifuging at 4000  $\times g$  for 5 min at 4 °C. AT46, AT47 and MAI-203 in plasma samples were analyzed using liquid chromatography coupled with tandem mass spectrometry (LC–MS/MS) method. The pharmacokinetic parameters were calculated using WinNonlin (Phoenix™, version 8.3) software.

#### 4.13. LC–MS/MS assay

LC–MS/MS analysis was performed using a Nexera LC-40 UHPLC (Shimadzu) system coupled with a Triple Quad 6500+

mass spectrometer (Sciex) with a HALO 90A AQ-C18 column (2  $\mu\text{mol/L}$ , 3.0 mm  $\times$  30 mm). The mobile phases were 5% acetonitrile in water with 0.1% formic acid (A) and 95% acetonitrile in water with 0.1% formic acid (B). The gradient elution was as follows: 0–0.2 min 20% B, 0.2–1.1 min 20%–100% B, 1.1–1.7 min 100% B. The flow rate was 0.6 mL/min. The injection volume was 10  $\mu\text{L}$ .

The mass spectrometry analysis was performed using negative multiple reaction monitoring (MRM) mode. The curtain gas (CUR), collision gas (CAD), ionspray voltage (IS), ionspray temperature (TEM), ion source gas 1 (GAS1) and ion source gas 2 (GAS2) for these compounds were 40 psi, 9 psi, –4500 V, 350  $^{\circ}\text{C}$ , 50 psi, 50 psi, respectively. The MRM transitions for AT46, AT47, MAI-203 and internal standard (IS) were 803.0/426.1, 858.2/84.1, 910.2/802.2 and 437.2/361.1, respectively. Data were acquired and analyzed using Analyst 1.7.3 (Sciex) software.

#### 4.14. *In vivo* lung metastasis assays

All animal experiments were performed following protocols approved by the Animal Ethics Committee of Shanghai Jiao Tong University. The mouse model of lung metastasis was established by tail-vein injection of SW480 cells into the BALB/c nude mice. After implantation of SW480 cells ( $1 \times 10^6$  per mice) in the tail vein of ten 5-week-old BALB/c nude mice for 14 days, all mice were randomly divided into two groups ( $n = 5$ ). One group administered intraperitoneally 2 mg/kg compound AT47 once daily for 2 weeks. The mice were sacrificed by cervical dislocation on Day 29 and the lung tissues were collected and fixed with phosphate-buffered formalin for subsequent pathological analysis. The lung metastasis was evaluated by the number of tumor metastases in the mice lung.

#### Acknowledgments

This work was funded by the National Key R&D Program of China (2023YFF1205103 to Jian Zhang), the Key Research and Construction Programs of Ningxia Hui Autonomous Region (2022BEG01002 to Jian Zhang, China), the Starry Night Science Fund of Zhejiang University Shanghai Institute for Advanced Study (SN-ZJU-SIAS-007 to Jian Zhang, China), the National Natural Science Foundation of China (22237005 and 81925034 to Jian Zhang), the open fund of state key laboratory of Pharmaceutical Biotechnology, Nanjing University (KF-202201 to Jian Zhang, China), the open fund of Basic Science Research Center Base (Pharmaceutical Science Y202203 to Xiuyan Yang, China).

#### Author contributions

Jian Zhang, Chen-Ying Liu and Ting Shi conceived and directed the project. Xuefei Wang designed and synthesized compounds and wrote the manuscript; Zeqian Du performed the molecular docking and ONIOM model analysis; Yuegui Guo contributed to the cell and animal experiments; Jie Zhong contributed to the *in vitro* biology experiments. Kun Song determined the crystal structure; Junyuan Wang contributed to compounds purification; Xiuyan Yang and Jianqiang Yu reviewed the paper; All authors provided critical feedback and have approved the final version of the manuscript.

#### Conflicts of interest

The authors declare no conflicts of interest.

#### Appendix A. Supporting information

Supporting data to this article can be found online at <https://doi.org/10.1016/j.apsb.2024.03.020>.

#### References

- Siegel RL, Miller KD, Fuchs HE, Jemal A. Cancer statistics, 2022. *CA Cancer J Clin* 2022;**72**:7–33.
- Ciardiello F, Ciardiello D, Martini G, Napolitano S, Taberero J, Cervantes A. Clinical management of metastatic colorectal cancer in the era of precision medicine. *CA Cancer J Clin* 2022;**72**:372–401.
- Zeineddine FA, Zeineddine MA, Yousef A, Gu Y, Chowdhury S, Dasari A, et al. Survival improvement for patients with metastatic colorectal cancer over twenty years. *NPJ Precis Oncol* 2023;**7**:16.
- Morris VK, Kennedy EB, Baxter NN, Benson AB, Cercek A, Cho M, et al. Treatment of metastatic colorectal cancer: ASCO Guideline. *J Clin Oncol* 2023;**41**:678–700.
- Cassidy S, Syed BA. Colorectal cancer drugs market. *Nat Rev Drug Discov* 2017;**16**:525–6.
- Grothey A, Fakih M, Taberero J. Management of BRAF-mutant metastatic colorectal cancer: a review of treatment options and evidence-based guidelines. *Ann Oncol* 2021;**32**:959–67.
- Shin AE, Giancotti FG, Rustgi AK. Metastatic colorectal cancer: mechanisms and emerging therapeutics. *Trends Pharmacol Sci* 2023;**44**:222–36.
- Cremolini C, Schirripa M, Antoniotti C, Moretto R, Salvatore L, Masi G, et al. First-line chemotherapy for mCRC—a review and evidence-based algorithm. *Nat Rev Clin Oncol* 2015;**12**:607–19.
- Aparicio J, Esposito F, Serrano S, Falco E, Escudero P, Ruiz-Casado A, et al. Metastatic colorectal cancer. First line therapy for unresectable disease. *J Clin Med* 2020;**9**:3889–99.
- Rowan AJ, Lammler H, Ilyas M, Wheeler J, Straub J, Papadopoulos A, et al. APC mutations in sporadic colorectal tumors: a mutational "hotspot" and interdependence of the "two hits". *Proc Natl Acad Sci U S A* 2000;**97**:3352–7.
- Bugter JM, Fenderico N, Maurice MM. Mutations and mechanisms of WNT pathway tumour suppressors in cancer. *Nat Rev Cancer* 2021;**21**:5–21.
- Fodde R, Smits R, Clevers H. APC, signal transduction and genetic instability in colorectal cancer. *Nat Rev Cancer* 2001;**1**:55–67.
- Fodde R. The multiple functions of tumour suppressors: it's all in APC. *Nat Cell Biol* 2003;**5**:190–2.
- Mitin N, Betts L, Yohe ME, Der CJ, Sondek J, Rossman KL. Release of autoinhibition of ASEF by APC leads to CDC42 activation and tumor suppression. *Nat Struct Mol Biol* 2007;**14**:814–23.
- Kawasaki Y, Senda T, Ishidate T, Koyama R, Morishita T, Iwayama Y, et al. Asef, a link between the tumor suppressor APC and G-protein signaling. *Science* 2000;**289**:1194–7.
- Zhang Z, Chen L, Gao L, Lin K, Zhu L, Lu Y, et al. Structural basis for the recognition of Asef by adenomatous polyposis coli. *Cell Res* 2012;**22**:372–86.
- Kawasaki Y, Sato R, Akiyama T. Mutated APC and Asef are involved in the migration of colorectal tumour cells. *Nat Cell Biol* 2003;**5**:211–5.
- Jiang H, Deng R, Yang X, Shang J, Lu S, Zhao Y, et al. Peptidomimetic inhibitors of APC–Asef interaction block colorectal cancer migration. *Nat Chem Biol* 2017;**13**:994–1001.
- Yang X, Zhong J, Zhang Q, Qian J, Song K, Ruan C, et al. Rational design and structure validation of a novel peptide inhibitor of the adenomatous-polyposis-coli (APC)-rho-guanine-nucleotide-exchange-factor-4 (Asef) interaction. *J Med Chem* 2018;**61**:8017–28.

20. Zhong J, Guo Y, Lu S, Song K, Wang Y, Feng L, et al. Rational design of a sensitivity-enhanced tracer for discovering efficient APC–Asef inhibitors. *Nat Commun* 2022;**13**:4961–75.
21. Kim GC, Cheon DH, Lee Y. Challenge to overcome current limitations of cell-penetrating peptides. *Biochim Biophys Acta, Proteins Proteomics* 2021;**1869**:140604–24.
22. Derakhshankhah H, Jafari S. Cell penetrating peptides: a concise review with emphasis on biomedical applications. *Biomed Pharmacother* 2018;**108**:1090–6.
23. Reissmann S. Cell penetration: scope and limitations by the application of cell-penetrating peptides. *J Pept Sci* 2014;**20**:760–84.
24. He H, Sun L, Ye J, Liu E, Chen S, Liang Q, et al. Enzyme-triggered, cell penetrating peptide-mediated delivery of anti-tumor agents. *J Control Release* 2016;**240**:67–76.
25. Reissmann S, Filatova MP. New generation of cell-penetrating peptides: functionality and potential clinical application. *J Pept Sci* 2021;**27**:3300–15.
26. Begley R, Liron T, Baryza J, Mochly-Rosen D. Biodistribution of intracellularly acting peptides conjugated reversibly to Tat. *Biochem Biophys Res Commun* 2004;**318**:949–54.
27. Szabó I, Yousef M, Soltész D, Bató C, Mező G, Bánóczy Z. Redesigning of cell-penetrating peptides to improve their efficacy as a drug delivery system. *Pharmaceutics* 2022;**14**:907–45.
28. Chang CE, Chen W, Gilson MK. Ligand configurational entropy and protein binding. *Proc Natl Acad Sci U S A* 2007;**104**:1534–9.
29. Head RD, Smythe ML, Oprea TI, Waller CL, Green SM, Marshall GR. VALIDATE: a new method for the receptor-based prediction of binding affinities of novel ligands. *J Am Chem Soc* 1996;**118**:3959–69.
30. Diehl C, Engström O, Delaine T, Håkansson M, Genheden S, Modig K, et al. Protein flexibility and conformational entropy in ligand design targeting the carbohydrate recognition domain of galectin-3. *J Am Chem Soc* 2010;**132**:14577–89.
31. Caro JA, Harpole KW, Kasinath V, Lim J, Granja J, Valentine KG, et al. Entropy in molecular recognition by proteins. *Proc Natl Acad Sci U S A* 2017;**114**:6563–8.
32. Jia Y, Wang J, Li P, Ma X, Han K. Directionally modified fluorophores for super-resolution imaging of target enzymes: a case study with carboxylesterases. *J Med Chem* 2021;**64**:16177–86.
33. Heard KR, Wu W, Li Y, Zhao P, Woznica I, Lai JH, et al. A general method for making peptide therapeutics resistant to serine protease degradation: application to dipeptidyl peptidase IV substrates. *J Med Chem* 2013;**56**:8339–51.
34. Vered M, Burstein Y, Gertler A. Digestion of elastin by porcine pancreatic elastase I and elastase II. *Int J Pept Protein Res* 1985;**25**:76–84.
35. De Rosa L, Capasso D, Diana D, Stefania R, Di Stasi R, Fattorusso R, et al. Metabolic and conformational stabilization of a VEGF-mimetic beta-hairpin peptide by click-chemistry. *Eur J Med Chem* 2021;**222**:113575–89.
36. Han Y, Zhang M, Lai R, Zhang Z. Chemical modifications to increase the therapeutic potential of antimicrobial peptides. *Peptides* 2021;**146**:170666–84.
37. Lai Z, Yuan X, Chen H, Zhu Y, Dong N, Shan A. Strategies employed in the design of antimicrobial peptides with enhanced proteolytic stability. *Biotechnol Adv* 2022;**59**:107962–75.
38. Ding D, Xu S, da Silva-Júnior EF, Liu X, Zhan P. Medicinal chemistry insights into antiviral peptidomimetics. *Drug Discov Today* 2023;**28**:103468–81.
39. Hohenstein EG, Sherrill CD. Effects of heteroatoms on aromatic pi–pi interactions: benzene-pyridine and pyridine dimer. *J Phys Chem A* 2009;**113**:878–86.
40. Yan XQ, Wang ZC, Qi PF, Li G, Zhu HL. Design, synthesis and biological evaluation of 2-H pyrazole derivatives containing morpholine moieties as highly potent small molecule inhibitors of APC–Asef interaction. *Eur J Med Chem* 2019;**177**:425–47.
41. Ni D, Li Y, Qiu Y, Lu S, Zhang J. Combining allosteric with orthosteric drugs to overcome drug-resistance. *Trends Pharmacol Sci* 2020;**41**:336–48.
42. Li S, Zhang J, Lu S, Huang W, Geng L, Shen Q, et al. The mechanism of allosteric inhibition of protein tyrosine phosphatase 1B. *PLoS One* 2014;**9**:e97668.
43. Wang X, Ni D, Liu Y, Lu S. Rational design of peptide-based inhibitors disrupting protein–protein interactions. *Front Chem* 2021;**9**:682675–703.
44. Meyer EA, Castellano RK, Diederich F. Interactions with aromatic rings in chemical and biological recognition. *Angew Chem Int Ed Engl* 2003;**42**:1210–50.
45. Riwar LJ, Trapp N, Kuhn B, Diederich F. Substituent effects in parallel-displaced pi–pi stacking interactions: distance matters. *Angew Chem Int Ed Engl* 2017;**56**:11252–7.
46. Sherrill CD. Energy component analysis of pi interactions. *Acc Chem Res* 2013;**46**:1020–8.
47. Milton M, Deng R, Mann A, Wang C, Tang D, Weck M. Secondary structure in nonpeptidic supramolecular block copolymers. *Acc Chem Res* 2021;**54**:2397–408.
48. Ren X, Zhou J, Wang E, Yang T, Xu Z, Sisourat N, et al. Ultrafast energy transfer between pi-stacked aromatic rings upon inner-valence ionization. *Nat Chem* 2022;**14**:232–8.
49. Dai W, Jochmans D, Xie H, Yang H, Li J, Su H, et al. Design, synthesis, and biological evaluation of peptidomimetic aldehydes as broad-spectrum inhibitors against enterovirus and SARS-CoV-2. *J Med Chem* 2022;**65**:2794–808.
50. Wang L, Wang N, Zhang W, Cheng X, Yan Z, Shao G, et al. Therapeutic peptides: current applications and future directions. *Signal Transduct Targeted Ther* 2022;**7**:48–69.
51. Lenci E, Trabocchi A. Peptidomimetic toolbox for drug discovery. *Chem Soc Rev* 2020;**49**:3262–77.
52. Zhang G, Brown JS, Quararo J, Li C, Tan X, Hanna S, et al. Rapid de novo discovery of peptidomimetic affinity reagents for human angiotensin converting enzyme 2. *Commun Chem* 2022;**5**:8–23.
53. Liu X, Lu S, Song K, Shen Q, Ni D, Li Q, et al. Unraveling allosteric landscapes of allosterome with ASD. *Nucleic Acids Res* 2019;**48**:394–401.
54. Lu S, Chen Y, Wei J, Zhao M, Ni D, He X, et al. Mechanism of allosteric activation of SIRT6 revealed by the action of rationally designed activators. *Acta Pharm Sin B* 2021;**11**:1355–61.
55. Witte J, Goldey M, Neaton JB, Head-Gordon M. Beyond Energies: geometries of nonbonded molecular complexes as metrics for assessing electronic structure approaches. *J Chem Theor Comput* 2015;**11**:1481–92.